JPhys Materials

PAPER

Mo doped TiO_2: impact on oxygen vacancies, anatase phase stability and photocatalytic activity

Vignesh Kumaravel[1,2,7], **Stephen Rhatigan**[3], **Snehamol Mathew**[1,2], **Marie Clara Michel**[3], **John Bartlett**[1,2], **Michael Nolan**[3,7], **Steven J Hinder**[4], **Antonio Gascó**[5], **César Ruiz-Palomar**[6], **Daphne Hermosilla**[6] and **Suresh C Pillai**[1,2,7]

[1] Nanotechnology and Bio-Engineering Research Group, Department of Environmental Science, School of Science, Institute of Technology Sligo, Ash Lane, Sligo, Ireland
[2] Centre for Precision Engineering, Materials and Manufacturing Research (PEM), Institute of Technology Sligo, Ash Lane, Sligo, Ireland
[3] Tyndall National Institute, University College Cork, Lee Maltings, Dyke Parade, Cork, Ireland
[4] The Surface Analysis Laboratory, Faculty of Engineering and Physical Sciences, University of Surrey, Guildford, Surrey, United Kingdom
[5] Department of Forest and Environmental Engineering and Management, School of Forest and Natural Environment Engineering, Universidad Politécnica de Madrid, Ciudad Universitaria, Madrid, Spain
[6] Department of Agricultural and Forest Engineering, School of Bioenergy, Agronomic, and Forest Industry Engineering, University of Valladolid, Campus Duques de Soria, Soria, Spain
[7] Authors to whom any correspondence should be addressed.

E-mail: Kumaravel.Vignesh@itsligo.ie, michael.nolan@tyndall.ie and Pillai.Suresh@itsligo.ie

Keywords: photocatalysis, nanomaterials, TiO_2

Supplementary material for this article is available online

OPEN ACCESS

RECEIVED
28 November 2019

REVISED
24 January 2020

ACCEPTED FOR PUBLICATION
10 February 2020

PUBLISHED
31 March 2020

Abstract

This work outlines an experimental and theoretical investigation of the effect of molybdenum (Mo) doping on the oxygen vacancy formation and photocatalytic activity of TiO_2. Analytical techniques such as x-ray diffraction (XRD), Raman, x-ray photoelectron spectroscopy (XPS) and photoluminescence (PL) were used to probe the anatase to rutile transition (ART), surface features and optical characteristics of Mo doped TiO_2 (Mo–TiO_2). XRD results showed that the ART was effectively impeded by 2 mol% Mo doping up to 750 °C, producing 67% anatase and 33% rutile. Moreover, the crystal growth of TiO_2 was affected by Mo doping via its interaction with oxygen vacancies and the Ti–O bond. The formation of Ti–O–Mo and Mo–Ti–O bonds were confirmed by XPS results. Phonon confinement, lattice strain and non-stoichiometric defects were validated through the Raman analysis. DFT results showed that, after substitutional doping of Mo at a Ti site in anatase, the Mo oxidation state is Mo^{6+} and empty Mo-*s* states emerge at the titania conduction band minimum. The empty Mo-*d* states overlap the anatase conduction band in the DOS plot. A large energy cost, comparable to that computed for pristine anatase, is required to reduce Mo–TiO_2 through oxygen vacancy formation. Mo^{5+} and Ti^{3+} are present after the oxygen vacancy formation and occupied states due to these reduced cations emerge in the energy gap of the titania host. PL studies revealed that the electron–hole recombination process in Mo–TiO_2 was exceptionally lower than that of TiO_2 anatase and rutile. This was ascribed to introduction of 5*s* gap states below the CB of TiO_2 by the Mo dopant. Moreover, the photo-generated charge carriers could easily be trapped and localised on the TiO_2 surface by Mo^{6+} and Mo^{5+} ions to improve the photocatalytic activity.

1. Introduction

Titanium dioxide (TiO_2) has been identified as an interesting nanomaterial in the 21st century, owing to its promising physical, chemical and optical properties for numerous eco-friendly applications, such as water treatment, air purification, energy production and self-cleaning coatings using solar light [1]. The commercialisation of photocatalysis technology has gained significant interest in recent decades. The photocatalysis concept has been successfully established for various commercial products, such as cement [2], air purifier [3], paints [4], water filter [5], deodorisers [6], mosquito repellent fabrics [7], and antimicrobial

coatings [8, 9]. The most commonly existing crystalline polymorphs of TiO_2 are anatase, rutile and brookite [10–12]. Anatase is accepted to be the more active phase of TiO_2 and is preferred by the ceramic industries to fabricate light active antimicrobial indoor building materials such as ceramics, glass, tiles and sanitary surfaces [13, 14]. This requires thermal stability of the anatase phase under typical ceramic processing conditions. TiO_2 anatase is mainly fabricated at low calcination temperatures (~500 °C) to prevent the anatase to rutile phase transition (ART) [15–17], which produces the less photo-active rutile phase. The photo-activity of anatase arises from its appropriate band edge positions, electron affinity, ionisation potential, and the long lifetime of charge carriers [10, 12, 18]. Moreover, transient photo-conductance analysis has revealed that the electron–hole recombination phenomena in anatase (101) phase is much slower compared to rutile (110), which is credited in part to the indirect band gap of anatase [11, 19].

The unit cells of anatase and rutile phases are composed of TiO_6 octahedra with titanium atoms at the centre and oxygen atoms at the vertices [20]. Both anatase and rutile have a tetragonal primitive cell with space groups $I_{41/amd}$ for anatase and $P_{42/mnm}$ for rutile [20]. The octahedral structures of the anatase crystal has a distorted four edge sharing centre (4 corners and 4 edges), whereas the rutile owns a non-distorted two edge sharing centre (2 corners and 6 edges) [21]. The ART phase transformation is believed to occur via contraction of the *c*-axis, changes in lattice parameters and structural reformation (breaking and making of bonds) [13, 21]. TiO_2 anatase phase is easily prepared at a calcination temperature around 500 °C, owing to its low surface free energy [13, 20]. The phase transformation of TiO_2 mostly relies on surface defects (oxygen vacancies, Ti interstitials), crystal strain, particle size, existence of additives or dopants, and calcination conditions [20–22]. ART of TiO_2 at high temperature could be controlled by the addition of metal ions, suitable chemical modifiers and an appropriate synthesis method [13]. Doping with metal ions is a one of the profitable ways to retard the ART [14, 21, 23–31]. Metal ions could improve the thermal stability of TiO_2 through the reduction in contact points, and nucleation sites [32].

Generally, doping of an element with higher oxidation state compared to Ti^{4+} would improve charge carrier separation on the photocatalyst surface [33]. Molybdenum (Mo; with a highest oxidation state of Mo^{6+}) as a dopant is inexpensive, non-toxic and has high solubility in the TiO_2 anatase lattice [33]. The ionic radius of Mo^{6+} is almost identical to that of Ti^{4+}, being 0.062 nm and 0.068 nm, respectively, and, therefore, Mo^{6+} ions could easily replace Ti^{4+} ions in the anatase crystal lattice [34, 35]. This kind of doping would minimise the lattice distortion [35, 36]. Mo doping could also generate energy states within the band gap of TiO_2 to enhance the light absorption and minimise the electron–hole recombination [35–37]. Khan and Berk suggested that an impurity level of Mo^{6+}/Mo^{5+} (Mo^{6+} $4d^0$ $1e^- \rightarrow Mo^{5+}$ $4d^1$) could be generated below the conduction band (CB) of TiO_2. During photoexcitation, electron transition could occur from the 0 2*p* valence band (VB) of TiO_2 into the Mo^{6+}/Mo^{5+} impurity level and then to the CB of TiO_2 through *d*(Mo^{5+})–*d*(Ti) transition [38]. The photo-induced electrons could initiate the reduction of Ti^{4+} ions to Ti^{3+} states at the surface. Moreover, the calcination process creates oxygen vacancies. The substitution of Mo dopant in the TiO_2 crystal lattice could strongly influence the number of oxygen vacancies due to the charge compensation. The formation of Ti^{3+} surface defects and oxygen vacancies could amplify the photocatalytic efficiency of Mo–TiO_2 via creating new energy levels and capturing of CB electrons at the surface after the relaxation process [38].

Kemp and McIntyre [39] investigated the photocatalytic activity of Mo–TiO_2 for the degradation of polyvinylchloride. XRD results revealed that 34% of TiO_2 anatase content was retained by 1% Mo doping at a 600 °C calcination temperature. Fisher *et al* [40] studied the antimicrobial property of Mo–TiO_2 coated films on the soiled surfaces in a beer industry under visible light irradiation. The coatings were fabricated on a stainless steel substratum by a magnetron sputtering ion plating technique with the aim to avoid microbial fouling. The bacterium was selected through the isolation of microorganisms on the soiled surface. Mo–TiO_2 coated films showed five-log reduction against *Escherichia coli* under dark and light conditions. Mo–TiO_2 coatings could function as a secondary barrier to restrain the microbial contamination. Recently, Miljević *et al* [33] examined the photocatalytic (coated on glass substrate) and self-cleaning (coated on brick and stone) efficiency of Mo–TiO_2-layer double hydroxide (LDH) nanocomposite coatings under visible light irradiation. The results showed that the photocatalytic and self-cleaning properties of Mo–TiO_2-LDH (Mo/Ti = 0.03 mass ratio) were higher than that of TiO_2-LDH. After 24 h of light irradiation, the water contact angle (WCA) of Mo–TiO_2-LDH coated brick (87°) and stone (36°) was significantly decreased as compared to uncoated brick (105°) and stone (58°), suggesting hydrophilicity of the coating. In another study, Yoon *et al* [41] reported the photocatalytic activity of transparent Mo–TiO_2 (Mo = 3 at%) films templated using cellulose nanocrystals (CNCs). The optical analysis showed that the visible light absorption capability of Mo–TiO_2-CNCs was significantly higher than bare TiO_2.

The above studies show that Mo is a potential dopant to improve the photocatalytic performance of TiO_2. Mo doping could influence the surface characteristics, oxygen vacancies, crystallinity and formation of Ti^{3+} centres, however, there is still no comprehensive studies on the antimicrobial activity of high temperature stable anatase Mo–TiO_2. Thus, the focus of the present investigation is to study systematically the influence of Mo

doping on the phase stability of anatase, formation of oxygen vacancies, and the photocatalytic activity to show that Mo doping could preserve the anatase content at high calcination temperature and thus enhance the activity of TiO_2. A comprehensive analysis on the relationship between the dopant concentration and the surface characteristics of TiO_2 is discussed. Electron–hole recombination was studied through photoluminescence (PL) spectra. Density functional theory (DFT) calculations were also performed to examine the Mo oxidation state and the formation energy of oxygen vacancies and its role in the oxidation states of the cations and the resulting electronic structure, which is vital for the photocatalytic activity. The photocatalytic activity of Mo-doped anatase was studied using the disinfection of total bacteria in wastewater under UVA-LED light irradiation. The result demonstrates that Mo is a significant dopant to enhance the photocatalytic activity of TiO_2 anatase.

2. Materials and methods

Analytical grade chemicals were used in this study. All the chemicals were used as received without further purification.

2.1. Synthesis of Mo–TiO_2

In a typical procedure to prepare 0.5 mol% Mo–TiO_2, titanium isopropoxide (TTIP; 41.81 ml) was mixed with isopropanol (200 ml) under stirring for 15 min, denoted as solution A. In the meantime, solution B was prepared by mixing 0.1225 g of ammonium molybdate tetrahydrate ($(NH_4)_6Mo_7O_{24}.4H_2O$) in 200 ml of double distilled water under vigorous stirring for 15 min. Afterwards, solution B was added drop by drop into solution A to initiate the hydrolysis process under stirring for 30 min. The resultant milky white solution was dried at 100 °C for 24 h. The amorphous powders were then calcined at various temperatures (500 °C, 600 °C, 700 °C, 750 °C, and 800 °C) in a muffle furnace with a heating rate of 10 °C min^{-1} for 2 h. In a similar fashion, 1 mol%, 1.5 mol% and 2 mol% of Mo–TiO_2 samples were also synthesised. Pure TiO_2 (0 mol% Mo–TiO_2) was synthesised by the same procedure without addition of any Mo precursor.

2.2. DFT calculations

DFT calculations were executed by the VASP 5.4 [42, 43] code, using projector augmented wave [44, 45] (PAW) potentials to describe the core-valence interaction. The exchange-correlation functional is estimated by the Perdew-Wang functional (PW91) [46]. The potentials for titanium (Ti), oxygen (O) and molybdenum (Mo) explicitly account for 12, 6 and 12 valence electrons, respectively. The energy cut-off for the plane wave basis set is 400 eV and the convergence criteria for electronic and ionic relaxations are 10^{-4} eV and 0.02 eV $Å^{-1}$. The bulk lattice parameters of the anatase unit cell were computed as: $a = 3.791$ Å and $c = 9.584$ Å; these compare with experimental values of $a = 3.785$ Å and $c = 9.514$ Å [47]. A $(3 \times 3 \times 1)$ anatase supercell, with 108 atoms, was constructed using the computed lattice parameters given above for undoped anatase and Mo was substitutionally doped at a Ti site to give a dopant concentration of 2.8 at%.

A $(3 \times 3 \times 4)$ k-point sampling grid was used. The calculations were spin-polarised and no symmetry constraints were imposed. The calculations implemented an on-site Hubbard correction (DFT + U) [48, 49] to describe the partially filled Ti 3d and Mo 4d states; $U = 4.5$ eV is applied to Ti 3d states and $U = 4.0$ eV is applied to Mo 4d with these choices for U informed by previous studies [50–54].

We considered reduction of Mo-doped TiO_2 via oxygen vacancy formation. To identify the most stable site for vacancy formation, multiple oxygen sites of the Mo-doped structure were considered, taking into account the symmetry of the system. For each oxygen site the vacancy formation energy was computed from the following equation:

$$E^{vac} = E(Mo_xTi_{1-x}O_{2-y}) + 1/2E(O_2) - E(Mo_xTi_{1-x}O_2), \quad (1)$$

where $E(Mo_xTi_{1-x}O_{2-y})$ denotes the total energy of Mo–TiO_2 with a single oxygen vacancy. $E(Mo_xTi_{1-x}O_2)$ represents the total energy of Mo–TiO_2 without an oxygen vacancy. The oxygen vacancy formation energy is referenced to half the total energy of gas-phase O_2.

The oxidation states were analysed through Bader charge analysis [55] and computed spin magnetisations. Given the lack of such analysis in the available literature and to provide benchmark-computed values for the Bader charge of Mo in Mo–TiO_2, calculations were performed on bulk MoO_3 and MoS_2 as reference materials. In the former system, the Bader charge for Mo was computed as 9.2 electrons, to which we ascribe an oxidation state of Mo^{6+}; for the latter system, the computed Bader charge was 10.7 electrons, corresponding to Mo^{4+}.

2.3. Photocatalytic wastewater disinfection

The photocatalytic activity of Mo–TiO_2 (0.1 g l^{-1}) was assessed by the disinfection of microbes in wastewater (secondary effluent of an urban wastewater (WW) treatment plant, Medinaceli, Soria, Spain) under LED light

irradiation with different UVA wavelengths. The characteristics of effluent were determined by the standard methods of wastewater analysis (table S1 is available online at stacks.iop.org/JPMATER/3/025008/mmedia). The parameters such as pH, conductivity, total volatile solids, total suspended solids, chemical oxygen demand, and microbial count (*Escherichia coli*, non coliforms and other coliforms) were measured. Two parallel lines of 10 UVA LED lights (Seoul Viosys, Republic of Korea) of particular wavelength (385 and 395 nm), which were widely scattered to equally cover the reactor surface, was used as the irradiation source. 250 mA of current intensity was used in each LED light setup. This was equivalent to consuming 8.38 W and 8.25 W of electrical power by the 385 nm and 395 nm LED lights, respectively. The lamp was located at a distance of 4.5 cm from the water surface. Under this experimental condition, the actual irradiated power was determined by potassium ferrioxalate actinometry method [56, 57]. The results showed that 1682.8 ± 77.1 and 1607.7 ± 56.1 μmol m^{-2} s^{-1} of photons were emitted from the 385 and 395 nm LED lights, respectively. All the materials used in this experiment were previously sterilised in an autoclave at 100 °C and 1.5 bar for 40 min 100 ml of WW was treated in each trial in a glass reactor. 1.0 ml of aliquot was withdrawn from the photo-reactor at regular time intervals (such as 4, 8, 15, 30, 45, and 60 min) to measure the existence of bacteria, in terms of colony-forming units (CFU), by ISO 9308-1:2014 method [58].

At first, 0.5 ml of the WW sample was mixed with 0.5 ml of saline water (0.9 g l^{-1} NaCl in distilled water). Then the samples were filtrated through 0.45 μm white-gridded mixed cellulose ester filter (GN-6 Metricel®, Pall, New York, USA) in a laminar flow hood to avoid external contamination. Chromocult® agar plates (Millipore, Merck, Darmstadt, Germany) were used as the media to grow the bacterial colonies. CFUs were enumerated after incubating the plates at 36 °C ± 2 °C for 21–24 h. There are three types of colonies that may be identified to grow on Chromocult® agar plates such as *Escherichia coli* (dark-blue to violet colour); other coliforms, namely: *Enterobacter aerogenes*, *Citrobacter freundii*, (pink to red colour); and some non-coliform bacteria, namely: *Enterococcus faecalis*, *Pseudomonas aeruginosa* (colourless).

2.4. Characterisation

ART of Mo–TiO_2 was investigated with the help of x-ray diffraction (XRD) and Raman spectroscopy. The crystallinity and phase changes were studied through XRD (Siemens D500) using Cu Kα radiation (λ = 0.154 18 nm) in the 2θ range of 10°–80°. Spurr equation was applied to determine the anatase and rutile phase composition as follows:

$$F_R = \frac{1}{1 + 0.8[I_A(101)/I_R(110)]}, \tag{2}$$

where F_R, $I_A(101)$ and $I_R(110)$ are the rutile phase percentage, intensity of anatase peak and intensity of rutile peak, respectively. Scherrer equation was used to determine the average crystallite size. Raman spectra of Mo–TiO_2 samples were measured for an acquisition period of 3 s with a grating of 300 g mm^{-1}. The surface chemical composition, and the bonding interactions of Mo–TiO_2 were analysed using x-ray photoelectron spectroscopy (XPS) with K-alpha$^+$ spectrometer. PL analysis was recorded to study the effect of Mo doping on the lifetime of charge carriers (excitation wavelength of 350 nm).

3. Results and discussion

The lattice oxygen vacancies and the formation of energy levels in Mo–TiO_2 framework were studied via DFT calculations. The structural, optical and surface characteristics of Mo–TiO_2 were examined in detail using XRD, Raman, PL and XPS spectra. The phase percentages of Mo–TiO_2 at different calcination temperatures were investigated by XRD. The effect of Mo doping on the changes of TiO_2 lattice parameters were examined via Raman spectroscopy. The bonding interactions and oxygen vacancies were studied in detail by XPS and PL. Pure TiO_2 anatase (calcined at 500 °C) and rutile (calcined at 700 °C) were used as reference for comparison.

3.1. DFT

The relaxed structure of Mo-doped TiO_2 anatase is shown in figure 1(a). The computed Bader charge for Mo is 9.13 electrons, corresponding to Mo^{6+} based on comparisons with the Bader charge computed for Mo in bulk MoO_3. Mo–O distances are 1.94 Å and 2.01 Å for oxygen ions in equatorial and apical positions, respectively. These values are almost identical to those computed for Ti–O distances in the undoped supercell, 1.94 Å and 2.00 Å, owing to the similar ionic radii of Mo^{6+} and Ti^{4+}. Mo–O bond lengths are compared with experimentally determined Ti–O distances of 1.94 and 1.96 Å [47], for apical and equatorial oxygen sites.

We consider reduction of the system via oxygen vacancy formation as such defects are implicated in the ART [23, 59–61]. The most stable site for the formation of an oxygen vacancy is an equatorial site of the Mo-dopant and the relaxed geometry and excess spin density are shown in figure 1(b). The formation energy is 5.05 eV and this is more stable than the next most stable vacancy by 0.1 eV. By comparison, the vacancy formation energy in

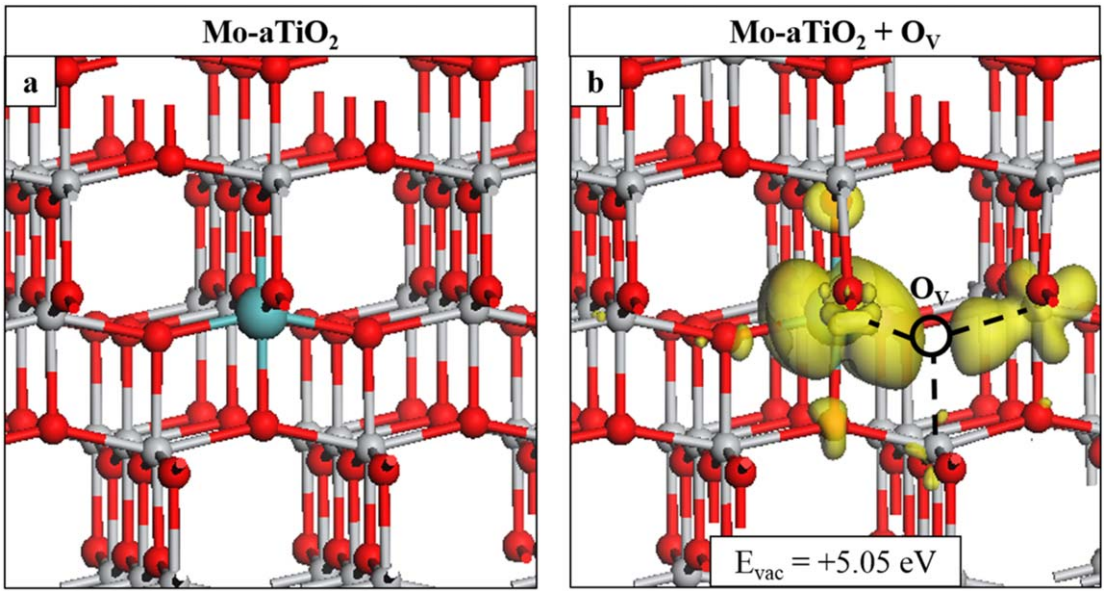

Figure 1. Relaxed geometry of Mo-doped TiO_2 anatase for (a) stoichiometric Mo–TiO_2 and (b) after formation of a single, reducing oxygen vacancy. The vacancy site sits at an equatorial position relative to the Mo-dopant and the formation energy is included in the inset of panel (b). The yellow iso-surface encloses spin densities of up to 0.02 eV $Å^{-3}$. The site of the removed O ion is indicated by the black circle and dashed black lines show the ions to which the removed oxygen was bound. In this and subsequent figures, Ti is represented by grey spheres, O by red and Mo by blue.

the undoped anatase supercell is 5.26 eV and so Mo-doping, at this concentration, will not promote vacancy formation to a significant degree.

After formation of a neutral oxygen vacancy, two electrons are released and these localise in the vicinity of the vacancy site, as shown in the excess spin density plot of figure 1(b). The computed Bader charge for Mo increases from 9.13 electrons, in the stoichiometric system, to 9.91 electrons in the reduced system, indicating reduction to Mo^{5+}. The spin magnetisation in the *d*-orbital of Mo is 1.1 μ_B. For one of the Ti ions to which the removed oxygen was bound, the Bader charge increases from 9.61 to 9.91 electrons. This Ti ion has a computed spin magnetisation of 0.2 μ_B. These results suggest that the excess charge occupies the vacancy site rather than localising at only the Mo and Ti ions (figure 1(b)). Typically, Ti^{3+} ions exhibit computed Bader charges of 10.0–10.5 electrons and spin magnetisations of 0.8–1.0 μ_B [23, 62]. The values computed for the partially reduced Ti ion in the present work are consistent with our previous study of In-doped TiO_2 [59]. This study showed excess charge distributed over the vacancy site in the reduced system, rather than localised at cation sites; the computed Bader charge and spin magnetisation for Ti sites neighbouring the vacancy were 9.7/9.8 electrons and 0.1/0.2 μ_B, respectively. The excess spin density plot in figure 1(b) shows that the charges are distributed over Mo and Ti and the electron density extends towards the vacancy site.

The projected electronic density of states (PEDOS) were computed for the stoichiometric and reduced system, with one oxygen vacancy, and these are shown in figure 2. For the stoichiometric system (figure 2(a)), Mo *s*-states emerge at the CBM of the TiO_2 host and the Mo *d*-states overlap with the titania CB. The emergence of Mo-derived defect states below the CBM was reported by the GGA studies of Mo-doped TiO_2 [36, 63]. Mo *d*-states below the CBM were identified in these studies but there was no discussion of the Mo *s*-states. In the present work, we find that Mo *d*-states lie above the CBM and this may be ascribed to the implementation of a Hubbard U on Mo *d*-states which shifts these states with respect to the TiO_2 CBM. After vacancy formation and reduction of Ti and Mo, occupied Ti and Mo *d*-states emerge in the band gap at 1.65 eV above the valence band maximum, as shown in figures 2(b) and (c).

3.2. XRD

XRD patterns of Mo–TiO_2 samples calcined at 600 °C, 700 °C, 750 °C and 800 °C are shown in figure 3. The results revealed that the anatase phase of TiO_2 is significantly preserved up to 750 °C by Mo doping [39] (table 1). A small red shift is observed for the anatase peak when the Mo content is increased from 0 to 2 mol%, suggesting the dopant-induced lattice distortion [38]. The intensity and width of anatase peaks are strongly influenced by Mo concentration. The average crystallite size of as-synthesised materials is given in table 2. For 600 °C, the average crystallite size of anatase is decreased with an increase of Mo content, indicating the crystal growth is restrained by Mo content. The existence of Mo ions in the TiO_2 lattice could distribute point defects as

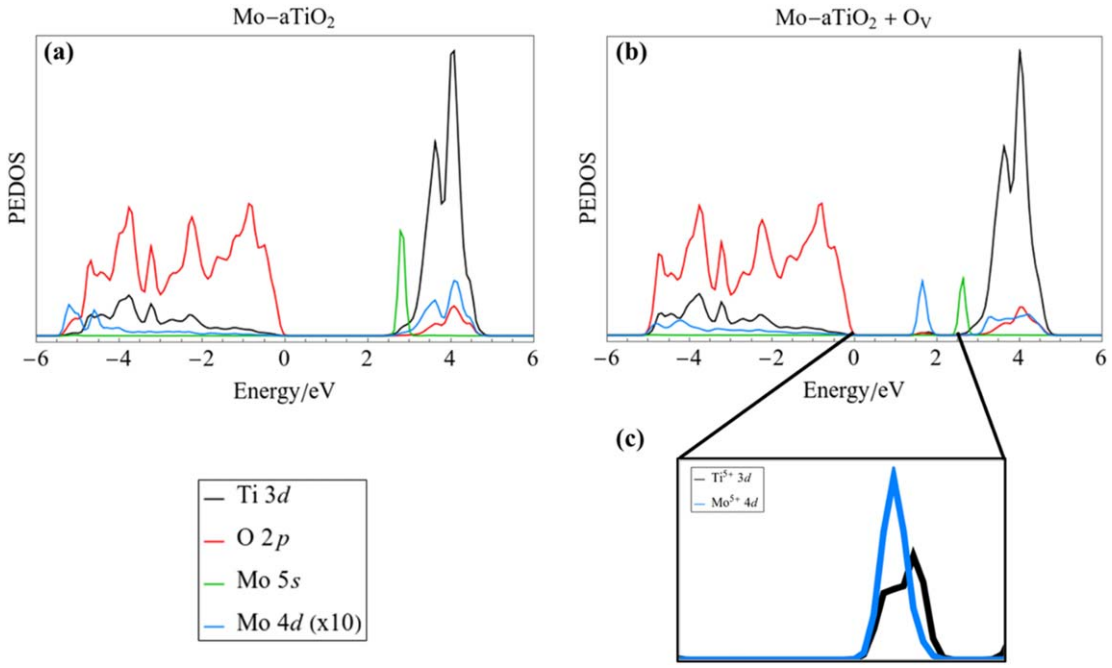

Figure 2. Computed PEDOS for (a) stoichiometric Mo-doped TiO_2 anatase and (b) reduced Mo-doped TiO_2 anatase, with one oxygen vacancy. Panel (c) shows the occupied Ti^{3+} and Mo^{5+} states which emerge in the band gap after vacancy formation.

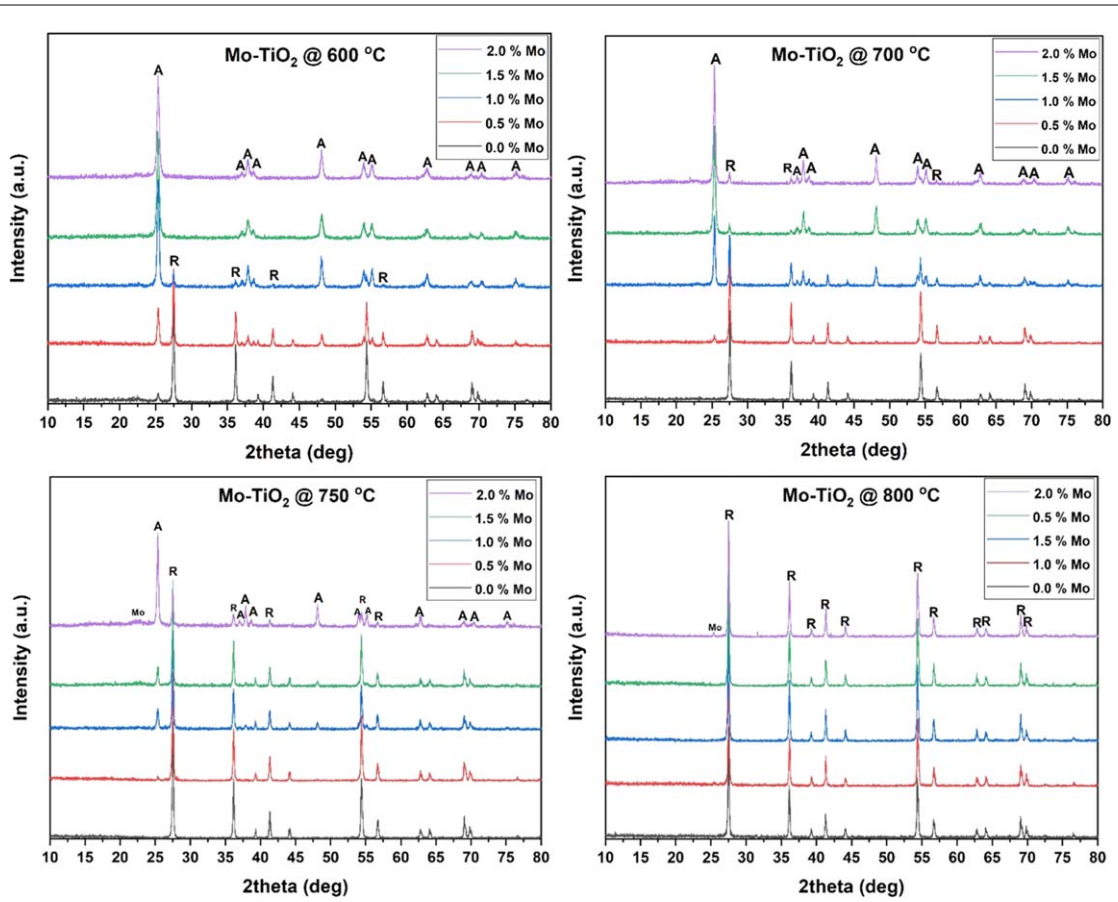

Figure 3. XRD patterns of Mo–TiO_2 at various calcination temperatures.

Table 1. The phase percentages of Mo–TiO_2 samples calcined at various temperatures.

	500 °C		600 °C		700 °C		750 °C		800 °C	
Samples	Anatase	Rutile	Anatase	Rutile	Anatase	Rutile	Anatase	Rutile	Anatase	Rutile
0.0% Mo–TiO_2	100	—	7	93	—	100	—	100	—	100
0.5% Mo–TiO_2	100	—	30	71	7	93	4	96	—	100
1.0% Mo–TiO_2	100	—	84	16	52	48	15	85	—	100
1.5% Mo–TiO_2	100	—	100	—	87	13	14	86	—	100
2.0% Mo–TiO_2	100	—	100	—	87	13	67	33	—	100

Table 2. The average crystallite size of Mo–TiO_2.

		Particle size (nm)	
Sample	Temperature (°C)	Anatase	Rutile
0.0% Mo–TiO_2	600 °C	29.918	35.715
0.5% Mo–TiO_2	600 °C	24.908	34.734
1.0% Mo–TiO_2	600 °C	23.060	36.316
1.5% Mo–TiO_2	600 °C	19.129	—
2.0% Mo–TiO_2	600 °C	18.729	—
0.0% Mo–TiO_2	700 °C	—	36.234
0.5% Mo–TiO_2	700 °C	24.246	36.899
1.0% Mo–TiO_2	700 °C	28.0769	35.430
1.5% Mo–TiO_2	700 °C	24.469	34.6589
2.0% Mo–TiO_2	700 °C	26.248	—
0.0% Mo–TiO_2	750 °C	—	36.661
0.5% Mo–TiO_2	750 °C	—	36.000
1.0% Mo–TiO_2	750 °C	28.0769	36.580
1.5% Mo–TiO_2	750 °C	38.0136	33.068
2.0% Mo–TiO_2	750 °C	28.0700	36.362

heterogeneous nucleation sites, which may restrict the crystal growth [41, 64]. Besides, the number of intergranular contacts between the nearby titania grains may decrease when increasing the concentration of Mo [38]. For 700 and 750 °C, the average crystallite size of TiO_2 anatase does not vary much with Mo mol% and the size is increased in some cases such as 1 mol% Mo–TiO_2 (700 °C) and 1.5 mol% Mo–TiO_2 (750 °C). The doping sites of TiO_2 are mainly decided through the ionic radii, coordination number and valence electron of the dopant [65]. The ionic radius of Mo^{6+} (0.062 nm) is close to that of Ti^{4+} (0.068 nm), hence Mo^{6+} could easily substitute Ti^{4+} ions in the anatase lattice, suggesting changes in lattice parameters and crystal plane distance [65–67]. The increase of Mo concentration above 2 mol% results in the formation of molybdenum trioxide (MoO_3). The major peaks of MoO_3 are analogous to those of anatase (101) and rutile (110) peaks. It could be difficult to distinguish the anatase crystalline peaks for samples with high Mo mol% (e.g. 4 mol%, 8 mol%, 16 mol%, etc). Consequently, 2 mol% of Mo is sufficient to maintain the anatase percentage of TiO_2 at high calcination temperatures.

3.3. XPS

The binding interactions and oxidation state of elements in Mo–TiO_2 were analysed by XPS. Ti 2*p*, O 1*s*, Mo 3*d* scans of pure TiO_2 (0 mol% Mo–TiO_2 at 500 °C) and 2 mol% Mo–TiO_2 at 750 °C are displayed in figure 4. The representative spin–orbit coupling of Ti 2*p* peaks such as Ti $2p_{3/2}$ and Ti $2p_{1/2}$ are observed at 458.86 eV and 464.53 eV, respectively (figure 4(a)) [68, 69]. This is ascribed to the existence of titanium in Ti^{4+} state. The O 1*s* spectrum of TiO_2 is composed of two peaks. O 1s peak is divided into two sub components by peak fitting. The peak located at 530.03 eV is attributed to lattice oxygen in Ti–O bond of TiO_2 [69]. The surface O–H group of TiO_2 is detected around 531.94 eV (figure 4(b)) [68, 69]. The peak positions of Ti 2*p* and O 1*s* are slightly increased for 2 mol% Mo–TiO_2 compared to pure TiO_2 (figures 4(c) and (d)). This is ascribed to high electronegativity of Mo compared to Ti, suggesting a lattice shift by the substitution of Mo^{6+} for Ti^{4+} ion [34]. Oxygen vacancies would also be created by this kind of replacement [34, 68], however, this was not observed in our DFT calculations. Moreover, Mo ions may strongly interact with oxygen atoms or oxygen vacancies via chemical bonds in the anatase crystal lattice, suggesting the formation of structural defects such as Ti–O–Mo and Mo–Ti–O bonds by Mo doping [35].

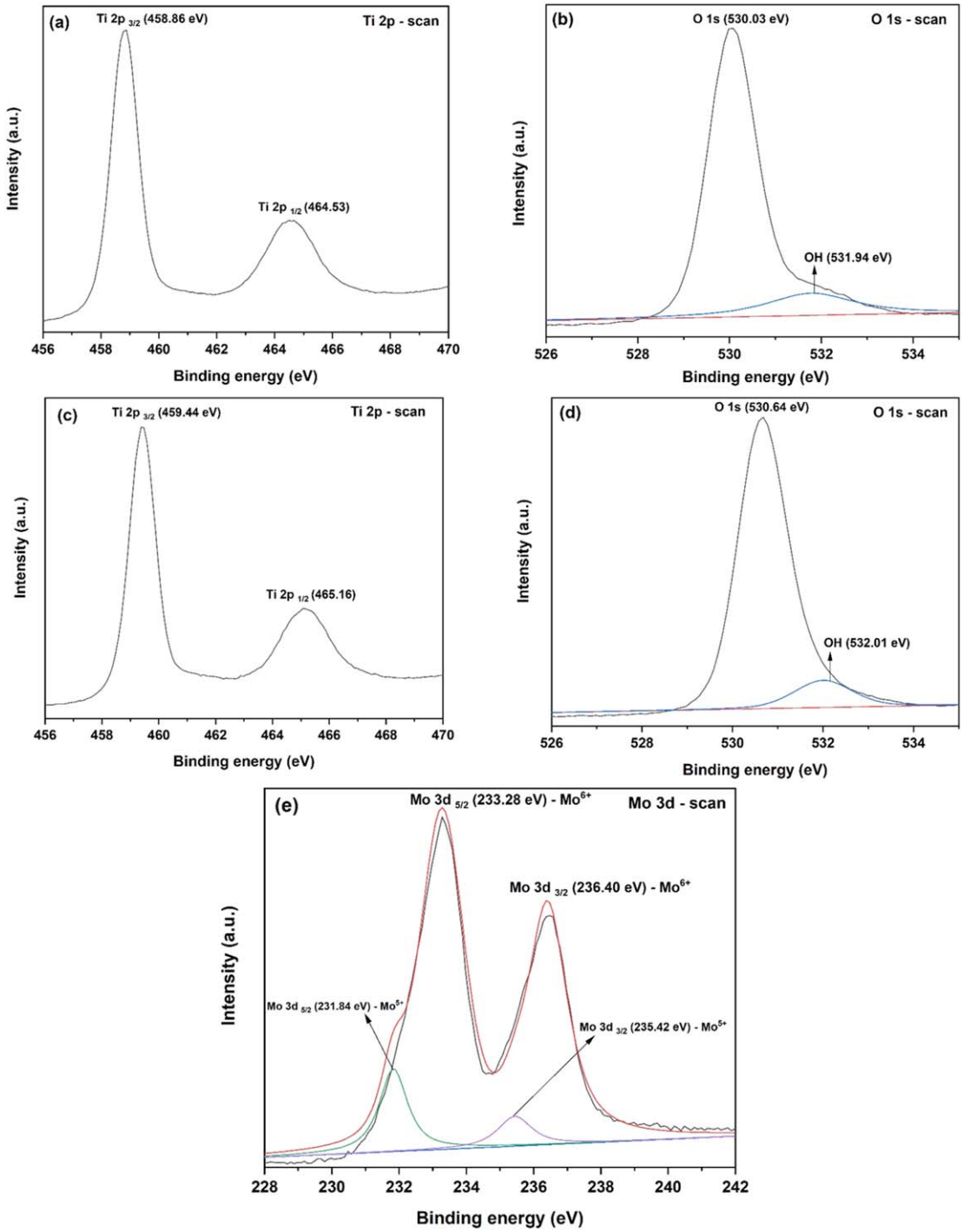

Figure 4. XPS of 0 mol% Mo–TiO_2 at 500 °C ((a) Ti 2*p* and (b) O 1*s*) and 2 mol% Mo–TiO_2 at 750 °C ((c) Ti 2*p* (d) O 1*s* (e) Mo 3*d*).

The peaks observed at 233.28 eV and 236.40 eV are accredited to Mo $3d_{5/2}$ and Mo $3d_{3/2}$ of Mo^{6+} (figure 4(e)). The sub components detected by peak fitting at 231.84 eV and 235.42 eV are ascribed to Mo $3d_{5/2}$ and Mo $3d_{3/2}$ of Mo^{5+}. XPS results showed that the percentage of Mo^{6+} is higher than that of Mo^{5+}. The existence of Mo^{5+} denotes that the oxygen atoms in the anatase lattice are inadequate to reinforce Mo^{6+} ions [35] and based on DFT calculations this is consistent with reduction to Mo^{5+} after O_V formation. A gap state (5*s* state of Mo) may be generated below the CB of TiO_2 by Mo doping. This is beneficial to restrain the electron–hole recombination process and prolong the life time of charge carriers. The oxidation-reduction potential of Ti^{4+}/Ti^{3+} (0.1 eV) is lower than that of Mo^{6+}/Mo^{5+} (0.4 eV) [38]. During light irradiation, Mo^{6+} could react with photo-induced hole to form Mo^{7+}, which is highly unstable. Consequently Mo^{7+} can further react with surface adsorbed –OH groups to generate $^{\cdot}OH$ and Mo^{6+} ($Mo^{7+} + OH^- \rightarrow Mo^{6+} + {}^{\cdot}OH$) [38].

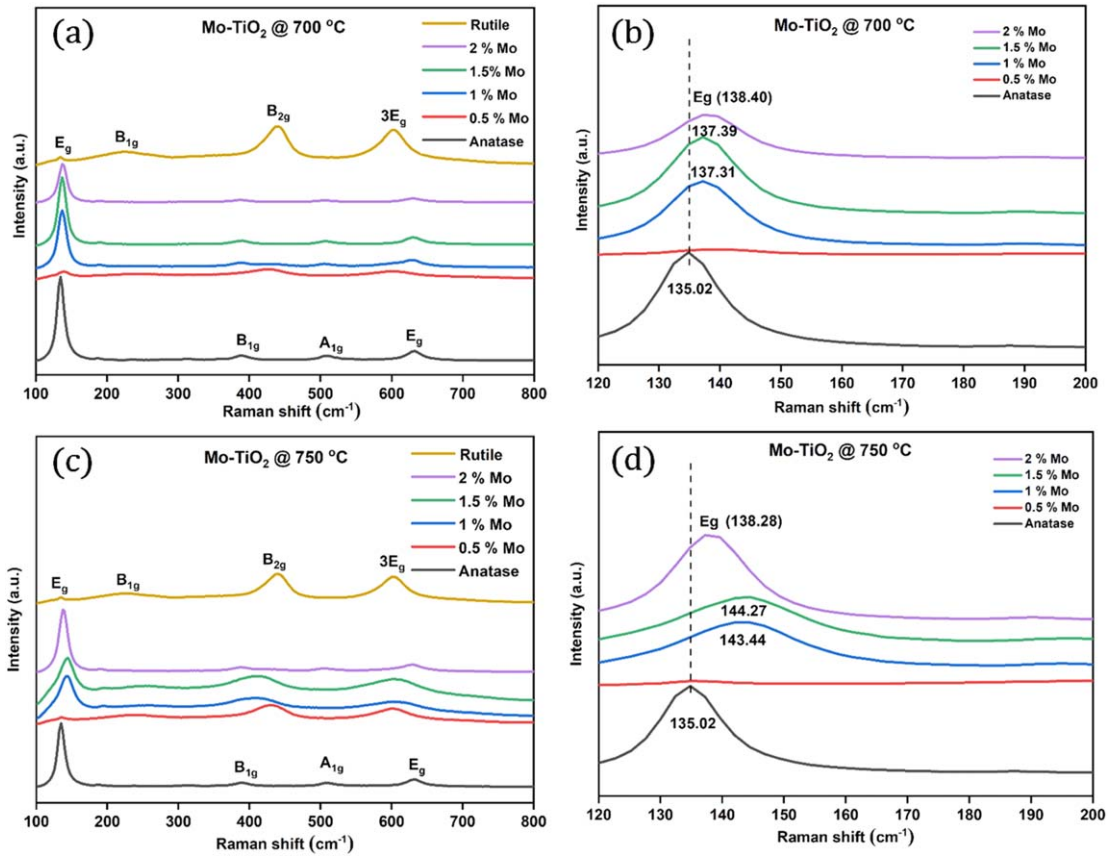

Figure 5. Raman spectra of (a) and (b) Mo–TiO_2 at 700 °C, (c) and (d) Mo–TiO_2 at 750 °C.

3.4. Raman spectra

The effect of Mo doping on the structural changes of TiO_2 anatase was interpreted through Raman spectroscopy. Figure 5 shows the Raman spectra of pure anatase (0 mol% TiO_2 calcined at 500 °C), rutile (0 mol% TiO_2 calcined at 700 °C) and Mo–TiO_2 samples (calcined at 700 °C and 750 °C). The results showed that Raman modes of TiO_2 anatase are strongly influenced by Mo doping. Raman modes such as E_g, B_{1g}, and A_{1g} are mainly originated from symmetric stretching O–Ti–O, symmetric bending O–Ti–O and anti-symmetric bending O–Ti–O vibrations, respectively [70]. Among them, E_g, and A_{1g} vibrations are more responsive to oxygen vacancies. Raman active modes of TiO_2 anatase (space group: $D^{19}{}_{4h}$ ($I_{41/amd}$)) and rutile (space group: $D^{14}{}_{4h}$ ($P_{42/mnm}$)) are observed at their corresponding positions. E_g, B_{1g}, A_{1g} or B_{1g} and E_g Raman bands belonging to anatase are observed around 135.02 cm^{-1}, 388.61 cm^{-1}, 508.18 cm^{-1} and 631.82 cm^{-1}, respectively (table S2). The significant Raman bands associated with rutile are noted around 439.26 cm^{-1} and 602.94 cm^{-1}, respectively. As compared to pure anatase, the E_g peaks of Mo–TiO_2 are red shifted with an increase of line width [71]. The peak shift is explained by a number of competitive mechanisms, such as phonon confinement, lattice strain/distortion and non-stoichiometric defects due to oxygen vacancies [72–75]. The peak broadening of E_g with respect to the concentration of Mo is ascribed to changes in anatase crystal lattice, and the cleavage of vibrational phonon mode [76]. According to the Heisenberg uncertainty principle, the phonon momentum of distribution (ΔP) increases when the particle size decreases [73]. Consequently, the changes in particle size may influence the phonon frequency of Raman modes, leading to peak broadening [73]. As the Mo content is increased, the number of oxygen atoms to create Ti–O bonds is reduced, indicating a decrease in force constant of the bond [73]. This could induce a red shift of Raman peak, because the force constant of a band is inversely proportional to its wavenumber [73]. Choudhury *et al* [73] suggested that the red shift is related to the reduced lattice size and diminishing of Ti–O bond. Liu and Syu [77] indicated that the red shift and peak broadening are attributed to oxygen deficiency in the crystal.

3.5. PL

PL spectra of Mo–TiO_2 samples calcined at 700 °C are shown in figure 6. Mechanisms such as electron–hole recombination or separation and electron–phonon scattering are involved in the PL process [78]. PL spectrum of TiO_2 anatase primarily originates from oxygen vacancies, surface defects, and self-trapped excitons [78]. A

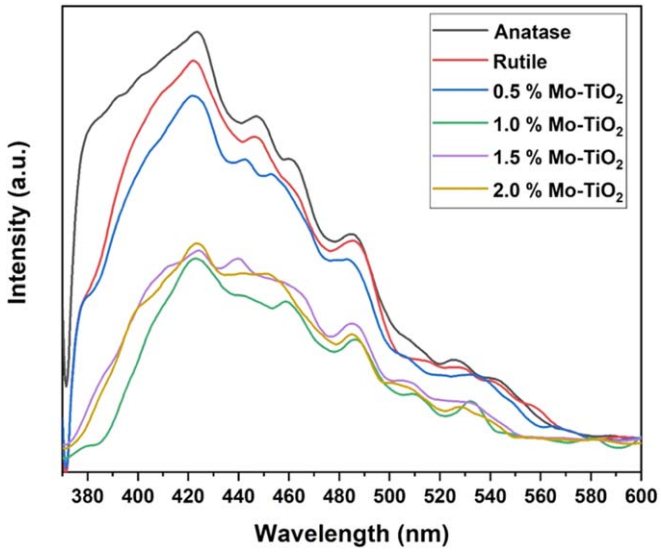

Figure 6. PL spectra of Mo–TiO_2, anatase and rutile.

peak at ca. 380 nm is ascribed to the band–band transition in TiO_2 [79, 80]. The characteristic radiative recombination of self-trapped excitons confined within the TiO_6 octahedra and oxygen vacancies is observed as a broad shoulder peak at ca. 419 nm [80]. The peaks found in the range of 400–500 nm originated from the oxygen vacancy related defect centres [80]. The blue-green emission peak observed around 485 nm is accredited to the charge transfer from Ti to O atom in TiO_6 octahedra associated with the oxygen vacancies [78]. The peaks at ca. 460 nm and 535 nm are correlated to trapped or bound electrons to the oxygen vacancy centres [79]. PL peak in the range of 485–490 nm is ascribed to the charge transfer process from Ti^{3+} to oxygen anion in TiO_6^{-8} complex coupled with surface oxygen vacancies [38]. The defect states or oxygen vacancy colour centres are denoted as F, F^+ and F^{2+} for two-trapped electrons, one-trapped electron and no-trapped electrons, respectively [79, 80]. PL quenching or enhancing mechanism results from the non-radiative oxygen vacancy colour centres. The peaks around 440 nm and 450 nm are associated to F or F^{2+} colour centres [80]. The dominant peaks around 460 nm and 485 nm are ascribed to F^+ colour centre [80].

In our samples, it is clear that the PL emission peaks of pure TiO_2 are quenched by introduction of the Mo dopant. The intensity of the PL peaks of the as-synthesised samples are in the order anatase (0% Mo–TiO_2 at 500 °C) > rutile (0% Mo–TiO_2 at 700 °C) > 0.5 Mo–TiO_2 > 2 Mo–TiO_2 > 1.5 Mo–TiO_2 > 1 Mo–TiO_2. Mo doping can introduce gap states below the CB of TiO_2 and this could suppress the electron–hole recombination process. The effect of Mo concentration on oxygen vacancies is clearly observed in terms of PL peak shift. Ti–O bond in the anatase lattice is disturbed by Mo doping. The impact on oxygen vacancies of TiO_2 could be attributed to the effect of calcination temperature [38]. The concentration of oxygen vacancy centres may vary with respect to the concentration of Mo [79]. Consequently, the photo-generated electrons could be easily trapped and localised in the oxygen vacancies, reducing the probability of photo-generated electron–hole recombination [79]. In addition to oxygen vacancies, the PL intensity could also be influenced through the mobility of carriers [79].

3.6. Photocatalytic wastewater disinfection

The photocatalytic activity of 0% mol Mo–TiO_2 (calcined at 500 °C) and 2% mol Mo–TiO_2 (calcined at 750 °C) for the specific removal of total bacteria in WW under 385 nm and 395 nm UVA LED light irradiation is displayed in figure 7. The percentages of N/N_0 values were plotted against the irradiation time. N and N_0 are the number of bacteria (CFU/ml) at irradiation time 't' and 0, respectively. The efficiency was denoted by a parameter 'b' (rate coefficient) from the exponential decay curves. In the case of 385 nm LED light, the total bacteria removal for 2% mol Mo–TiO_2 is ~1.5 times higher than that of TiO_2. However, the total bacteria removal for 2% mol Mo–TiO_2 is ~2.8 times higher in comparison with pure TiO_2 under 395 nm LED light irradiation. The disinfection efficiency of Mo–TiO_2 is maximal at 395 nm LED light compared to that of 385 nm LED light. The total disinfection was achieved in almost 30 min of LED light irradiation. The high activity of Mo–TiO_2 under 395 nm LED light is attributed to the maximum light absorption with respect to its specific band gap and electronic properties, suggesting the generation of more charge carriers responsible for microbial disinfection [81]. The photocatalytic activity could be influenced by the competitive reaction between the

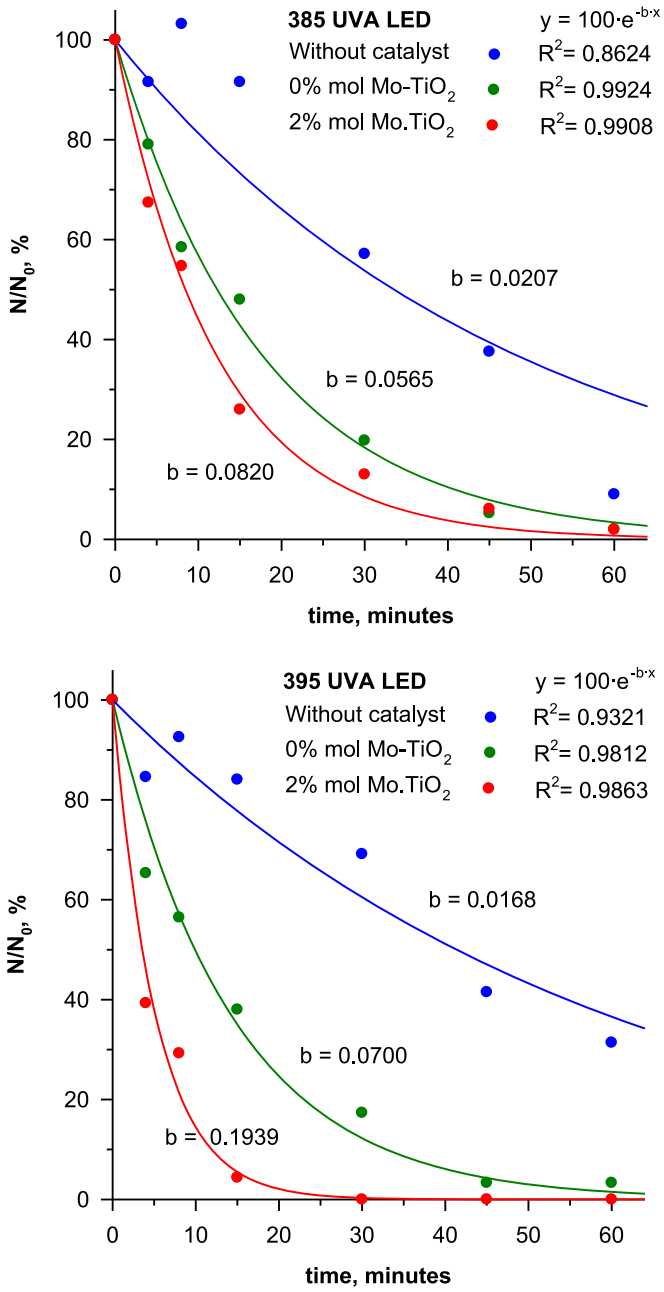

Figure 7. Photocatalytic disinfection efficiency of TiO_2 and Mo–TiO_2 under UVA LED light irradiation.

microbes and other organic matter existing in the WW [82]. Mo doping could enhance the surface active sites and endorse the interfacial charge transfer process [81, 83]. The Mo dopant could influence the crystallite size and surface active sites of TiO_2 to promote the adsorption of microbes on the photocatalyst surface [84]. The formation gap states by Mo dopant could extend the lifetime of photo-induced charge carriers. The poor disinfection for photolysis experiments is ascribed to the protection of remaining active cells by the metabolites released from the destructed cells [83, 85]. The disinfection mechanism of microbes in WW may be attributed to the oxidative degradation of cells by reactive oxygen species, increase of cell permeability, leakage of minerals, DNA/RNA damage, and inhibition of protein synthesis [83, 86, 87].

XRD and Raman analysis clearly validate that the anatase crystal structure of TiO_2 is well sustained after doping with Mo at high calcination temperature. DFT studies showed that gap states (such as *s*- and *d*- states) could be created between the VB and CB of TiO_2, suggesting enhanced charge carrier separation on the photocatalyst surface. Raman analysis suggested that the lattice size and Ti–O bond strength are modified by Mo doping. The formation of oxygen vacancies may be varied with respect to the Mo dopant concentration because of the cleavage of more Ti–O bonds, indicating the contraction of O–Ti–O bond angle [73]. The photo-generated electrons could be captured by Mo^{6+}, impurity levels, Ti^{3+} centres, and shallow or deep traps [38]. The trapped electrons would further react with

surface adsorbed oxygen to create more reactive oxygen species [38]. PL analysis confirmed that the charge carrier mobility would be decreased as they interact with the dopants or defect centres, suggesting enhancement in the charge–carrier separation to improve the photocatalytic activity. Mo doping does not introduce any new peaks in the PL spectrum of TiO_2. Nevertheless, the PL intensity of Mo–TiO_2 peaks are smaller compared to anatase and rutile, suggesting the modification of surface defects and a reduction in the number of recombination centres [38]. The photocatalytic activity was tested for the disinfection of microbes in a real WW system rather than using a simulated wastewater system. The disinfection efficiency of Mo–TiO_2 was superior compared to pure TiO_2. The photocatalytic experiments also demonstrated that Mo doping could improve the photon absorption of TiO_2. The high photocatalytic activity of Mo–TiO_2 is accredited to, surface characteristics, crystallinity, formation of gap states, *d–d* electron transition, and the existence of high anatase content [34, 38].

4. Summary

The effect of Mo doping on oxygen vacancy formation, anatase phase stability and photocatalytic activity of TiO_2 has been successfully investigated. DFT calculations reveal that the Mo dopant is present in anatase as Mo^{6+}, and is incorporated into the lattice with no distortions to the geometry, due to the similar ionic radii of Mo^{6+} and Ti^{4+}. Analysis of the computed PEDOS plot for the stoichiometric system indicates that Mo 5*s* states emerge below the CBM of TiO_2. The computed energy required for oxygen vacancy formation in Mo–TiO_2 is comparable to that of un-doped anatase and, hence, vacancies should be present in the doped system in similar concentrations to pure anatase, under equivalent preparation conditions. After vacancy formation, the dopant is reduced to Mo^{5+} and Ti^{3+} is also present. This leads to the emergence of occupied Mo 4*d* and Ti 3*d* states in the energy gap. The peak shift in the Raman spectra revealed the influence of oxygen vacancies on the anatase crystal lattice. XPS results show the existence of Mo^{5+} in addition to Mo^{6+} in Mo–TiO_2 samples. The formation of Ti–O–Mo and Mo–Ti–O bonds are also confirmed through XPS analysis. The results also suggest lattice distortions due to substitution of Mo^{6+} for Ti^{4+} ion. The electron transfer process between TiO_2 and surface oxygen vacancies is confirmed by PL analysis. The electron–hole recombination is minimised via the appearance of Mo electronic states below the CB of TiO_2. The life time of photo-induced charge carriers is extended through Mo^{6+}, impurity levels, and Ti^{3+} centres. The photocatalytic activity of Mo–TiO_2 was tested with a wastewater from a secondary effluent. The findings suggest that Mo–TiO_2 is an excellent candidate for the fabrication of indoor building materials with light active antimicrobial characteristics.

Acknowledgments

The authors are thankful to the Renewable Engine (RE) project funded by European Union's INTERREG VA Programme, managed by the Special EU Programmes Body (SEUPB), with match funding provided by the Department of Economy, Department of Jobs, Enterprise and Innovation in Ireland. S R and M N appreciate the support from Science Foundation Ireland (SFI) through the ERA.Net for Materials Research and Innovation (M-ERA.Net 2), SFI Grant Number SFI/16/M-ERA/3418 (RATOCAT) and Horizon 2020 grant (685451). We acknowledge the access to SFI funded computing resources at Tyndall Institute and the SFI/HEA funded Irish Centre for High End Computing. S R and M N are thankful to the COST Action CM1104 'Reducible Metal Oxides, Structure and Function' for the support. DH acknowledges '*Movilidad UVa-BANCO SANTANDER 2019*' mobility program for funding her research work at IT Sligo. CR-P participation in this work has been sponsored by the research initiative '*Cátedra de Conocimiento e Innovación*' from '*Caja Rural de Soria*' (Spain).

ORCID iDs

Vignesh Kumaravel https://orcid.org/0000-0003-4755-189X
Stephen Rhatigan https://orcid.org/0000-0002-9652-468X
Michael Nolan https://orcid.org/0000-0002-5224-8580
Antonio Gascó https://orcid.org/0000-0001-5832-7899
Daphne Hermosilla https://orcid.org/0000-0002-0006-2397
Suresh C Pillai https://orcid.org/0000-0002-8901-9116

References

[1] Kumaravel V, Mathew S, Bartlett J and Pillai S C 2019 Photocatalytic hydrogen production using metal doped TiO_2: a review of recent advances *Appl. Catal.* B **244** 1021–64
[2] Binas V, Papadaki D, Maggos T, Katsanaki A and Kiriakidis G 2018 Study of innovative photocatalytic cement based coatings: the effect of supporting materials *Constr. Build. Mater.* **168** 923–30

[3] Koivisto A J *et al* 2018 Dip coating of air purifier ceramic honeycombs with photocatalytic TiO_2 nanoparticles: a case study for occupational exposure *Sci. Total Environ.* **630** 1283–91
[4] Gandolfo A, Rouyer L, Wortham H and Gligorovski S 2017 The influence of wall temperature on NO_2 removal and HONO levels released by indoor photocatalytic paints *Appl. Catal.* B **209** 429–36
[5] Athanasekou C P *et al* 2015 Ceramic photocatalytic membranes for water filtration under UV and visible light *Appl. Catal.* B **178** 12–9
[6] Jo S-H, Kim K-H, Kim Y-H, Lee M-H, Kim B-W and Ahn J-H 2015 Deodorization of food-related nuisances from a refrigerator: the feasibility test of photocatalytic system *Chem. Eng. J.* **277** 260–8
[7] Abdelhameed R M, Kamel O M, Amr A, Rocha J and Silva A M 2017 Antimosquito activity of a titanium–organic framework supported on fabrics *ACS Appl. Mater. Interfaces* **9** 22112–20
[8] Leyland N S, Podporska-Carroll J, Browne J, Hinder S J, Quilty B and Pillai S C 2016 Highly efficient F, Cu doped TiO_2 anti-bacterial visible light active photocatalytic coatings to combat hospital-acquired infections *Sci. Rep.* **6** 24770
[9] Yemmireddy V K and Hung Y C 2017 Using photocatalyst metal oxides as antimicrobial surface coatings to ensure food safety—opportunities and challenges *Comprehensive Rev. Food Sci. Food Saf.* **16** 617–31
[10] Xia X *et al* 2018 Control of interface between anatase TiO_2 nanoparticles and rutile TiO_2 nanorods for efficient photocatalytic H2 generation *J. Power Sources* **376** 11–7
[11] Maity P, Mohammed O F, Katsiev K and Idriss H 2018 Study of the bulk charge carrier dynamics in anatase and rutile TiO_2 single crystals by femtosecond time-resolved spectroscopy *J. Phys. Chem.* C **122** 8925–32
[12] Dubey R 2018 Temperature-dependent phase transformation of TiO_2 nanoparticles synthesized by sol–gel method *Mater. Lett.* **215** 312–7
[13] Hanaor D A and Sorrell C C 2011 Review of the anatase to rutile phase transformation *J. Mater. Sci.* **46** 855–74
[14] Fagan R, Synnott D W, McCormack D E and Pillai S C 2016 An effective method for the preparation of high temperature stable anatase TiO_2 photocatalysts *Appl. Surf. Sci.* **371** 447–52
[15] Shirai K *et al* 2018 Water-assisted hole trapping at the highly curved surface of nano-TiO_2 photocatalyst *J. Am. Chem. Soc.* **140** 1415–22
[16] Xu F, Zhang J, Zhu B, Yu J and Xu J 2018 $CuInS_2$ sensitized TiO_2 hybrid nanofibers for improved photocatalytic CO_2 reduction *Appl. Catal.* B **230** 194–202
[17] Jia T, Fu F, Yu D, Cao J and Sun G 2018 Facile synthesis and characterization of N-doped TiO_2/C nanocomposites with enhanced visible-light photocatalytic performance *Appl. Surf. Sci.* **430** 438–47
[18] Kernazhitsky L, Shymanovska V, Gavrilko T, Naumov V, Fedorenko L and Baran J 2019 Dark-blue titanium dioxide: Effect of phenothiazine on structural and optical properties of nanocrystalline anatase TiO_2 *J. Phys. Chem. Solids* **126** 234–41
[19] Xu M *et al* 2011 Photocatalytic activity of bulk TiO_2 anatase and rutile single crystals using infrared absorption spectroscopy *Phys. Rev. Lett.* **106** 138302
[20] Yin W-J, Wen B, Zhou C, Selloni A and Liu L-M 2018 Excess electrons in reduced rutile and anatase TiO_2 *Surf. Sci. Rep.* **73** 58–82
[21] Khatun N *et al* 2018 Role of oxygen vacancies and interstitials on structural phase transition, grain growth, and optical properties of Ga doped TiO_2 *J. Appl. Phys.* **123** 245702
[22] Gaur L K *et al* 2019 Laser induced phase transformation influenced by Co doping in TiO_2 nanoparticles *J. Alloys Compd.* **780** 25–34
[23] Byrne C *et al* 2019 Effect of Cu doping on the anatase-to-rutile phase transition in TiO_2 photocatalysts: theory and experiments *Appl. Catal.* B **246** 266–76
[24] Nolan N T, Seery M K and Pillai S C 2009 Spectroscopic investigation of the anatase-to-rutile transformation of sol−gel-synthesized TiO_2 photocatalysts *J. Phys. Chem.* C **113** 16151–7
[25] da Silva L F, Avansi W Jr, Catto A C, Rodrigues J E, Bernardi M I and Mastelaro V R 2018 The role of Nb addition in TiO_2 nanoparticles: phase transition and photocatalytic properties *Phys. Status Solidi* a **215** 1800321
[26] Zanatta A, Scoca D and Alvarez F 2019 Influence of the Anatase and Rutile phases on the luminescent properties of rare-earth-doped TiO_2 films *J. Alloys Compd.* **780** 491–7
[27] Loan T T and Long N N 2019 Effect of Co^{2+} doping on Raman spectra and the phase transformation of TiO_2: Co^{2+} nanowires *J. Phys. Chem. Solids* **124** 336–42
[28] Zou K, Dong G, Liu J, Xu B and Wang D 2019 Effects of calcination temperature and Li + ions doping on structure and upconversion luminescence properties of TiO_2: Ho^{3+}–Yb^{3+} nanocrystals *J. Mater. Sci. Technol.* **35** 483–90.
[29] Arantes D C *et al* 2019 Effect of structural and Eu^{3+} amount in TiO_2 semiconductor material on downconversion photoluminescence properties *Opt. Mater.* **88** 522–33
[30] Suwannaruang T, Kidkhunthod P, Chanlek N, Soontaranon S and Wantala K 2019 High anatase purity of nitrogen-doped TiO_2 nanorice particles for the photocatalytic treatment activity of pharmaceutical wastewater *Appl. Surf. Sci.* **478** 1–14
[31] Zikriya M, Nadaf Y, Bharathy P V and Renuka C 2019 Luminescent characterization of rare earth Dy^{3+} ion doped TiO_2 prepared by simple chemical co-precipitation method *J. Rare Earths* **37** 24–31
[32] Feltrin J, De Noni A Jr, Hotza D and Frade J 2019 Design guidelines for titania-silica-alumina ceramics with tuned anatase to rutile transformation *Ceram. Int.* **45** 5179–88
[33] Miljević B, van der Bergh J, Vučetić S, Lazar D and Ranogajec J 2017 Molybdenum doped TiO_2 nanocomposite coatings: visible light driven photocatalytic self-cleaning of mineral substrates *Ceram. Int.* **43** 8214–21
[34] Zhang T, Yu B, Wang D and Zhou F 2015 Molybdenum-doped and anatase/rutile mixed-phase TiO_2 nanotube photoelectrode for high photoelectrochemical performance *J. Power Sources* **281** 411–6
[35] Erdogan N, Park J and Ozturk A 2016 Synthesis and enhanced photocatalytic activity of molybdenum, iron, and nitrogen triple-doped titania nanopowders *Ceram. Int.* **42** 16766–74
[36] Khan M, Xu J, Cao W and Liu Z-K 2014 Mo-doped TiO_2 with enhanced visible light photocatalytic activity: a combined experimental and theoretical study *J. Nanosci. Nanotechnol.* **14** 6865–71
[37] Zhou J, Feng B, Lu X and Duan K 2018 Novel one-step fabrication of highly ordered Mo-doped TiO_2 nanotubes arrays with enhanced visible light catalytic activity *J. Mater. Sci., Mater. Electron.* **29** 18388–96
[38] Khan H and Berk D 2014 Characterization and mechanistic study of Mo^{+6} and V^{+5} codoped TiO_2 as a photocatalyst *J. Photochem. Photobiol.* A **294** 96–109
[39] Kemp T J and McIntyre R A 2006 Transition metal-doped titanium (IV) dioxide: characterisation and influence on photodegradation of poly (vinyl chloride) *Polym. Degrad. Stab.* **91** 165–94
[40] Fisher L *et al* 2014 Molybdenum doped titanium dioxide photocatalytic coatings for use as hygienic surfaces: the effect of soiling on antimicrobial activity *Biofouling* **30** 911–9
[41] Yoon Y *et al* 2018 Photocatalytic performance of highly transparent and mesoporous molybdenum-doped titania films fabricated by templating cellulose nanocrystals *Ceram. Int.* **44** 16647–53

[42] Kresse G and Furthmüller J 1996 Efficiency of *ab-initio* total energy calculations for metals and semiconductors using a plane-wave basis set *Comput. Mater. Sci.* **6** 15–50
[43] Kresse G and Furthmüller J 1996 Efficient iterative schemes for *ab-initio* total-energy calculations using a plane-wave basis set *Phys. Rev.* B **54** 11169
[44] Kresse G and Joubert D 1999 From ultrasoft pseudopotentials to the projector augmented-wave method *Phys. Rev.* B **59** 1758–75
[45] Blöchl P E 1994 Projector augmented-wave method *Phys. Rev.* B **50** 17953–79
[46] Perdew J P, Burke K and Ernzerhof M 1996 Generalized gradient approximation made simple *Phys. Rev. Lett.* **77** 3865–8
[47] Rao K V K, Naidu S V N and Iyengar L 1970 Thermal expansion of rutile and anatase *J. Am. Ceram. Soc.* **53** 124–6
[48] Anisimov V I, Zaanen J and Andersen O K 1991 Band theory and Mott insulators: Hubbard u instead of stoner I *Phys. Rev.* B **44** 943–54
[49] Dudarev S L, Botton G A, Savrasov S Y, Humphreys C J and Sutton A P 1998 Electron-energy-loss spectra and the structural stability of nickel oxide: an LSDA + U study *Phys. Rev.* B **57** 1505–9
[50] Nolan M and Elliott S D 2006 The p-type conduction mechanism in Cu_2O: a first principles study *Phys. Chem. Chem. Phys.* **8** 5350–8
[51] Morgan B J and Watson G W 2007 A DFT + U description of oxygen vacancies at the TiO_2 rutile (1 1 0) surface *Surf. Sci.* **601** 5034–41
[52] Nolan M, Elliott S D, Mulley J S, Bennett R A, Basham M and Mulheran P 2008 Electronic structure of point defects in controlled self-doping of the TiO_2 (110) surface: combined photoemission spectroscopy and density functional theory study *Phys. Rev.* B **77** 235424
[53] Kowalski P M, Camellone M F, Nair N N, Meyer B and Marx D 2010 Charge localization dynamics induced by oxygen vacancies on the TiO_2 (110) surface *Phys. Rev. Lett.* **105** 146405
[54] Wu M *et al* 2018 Electronic structures, magnetic properties and band alignments of 3d transition metal atoms doped monolayer MoS_2 *Phys. Lett.* A **382** 111–5
[55] Henkelman G, Arnaldsson A and Jónsson H 2006 A fast and robust algorithm for Bader decomposition of charge density *Comput. Mater. Sci.* **36** 354–60
[56] Hatchard C and Parker C A 1956 A new sensitive chemical actinometer: II. Potassium ferrioxalate as a standard chemical actinometer *Proc. R. Soc.* A **235** 518–36
[57] Montalti M, Credi A, Prodi L and Gandolfi M T 2006 *Handbook of Photochemistry* (Boca Raton, FL: CRC Press)
[58] Lange B, Strathmann M and Oßmer R 2013 Performance validation of chromogenic coliform agar for the enumeration of *Escherichia coli* and coliform bacteria *Lett. Appl. Microbiol.* **57** 547–53
[59] Kumaravel V *et al* 2019 Indium doped TiO_2 photocatalysts with high temperature anatase stability *J. Phys. Chem.* C **123** 21083–96
[60] Pillai S C *et al* 2007 Synthesis of high-temperature stable anatase TiO_2 photocatalyst *J. Phys. Chem.* C **111** 1605–11
[61] Fagan R, McCormack D E, Hinder S and Pillai S C 2016 Improved high temperature stability of anatase TiO_2 photocatalysts by N, F, P co-doping *Mater. Des.* **96** 44–53
[62] Byrne C *et al* 2019 Modification of TiO_2 with hBN: high temperature anatase phase stabilisation and photocatalytic degradation of 1, 4-dioxane *J. Phys.: Mater.* **3** 015009
[63] Yu X, Hou T, Sun X and Li Y 2012 The influence of defects on Mo-doped TiO_2 by first-principles studies *Chem. Phys. Chem.* **13** 1514–21
[64] Liu G, Wang L, Yang H G, Cheng H-M and Lu G Q M 2010 Titania-based photocatalysts—crystal growth, doping and heterostructuring *J. Mater. Chem.* **20** 831–43
[65] Thi T V, Rai A K, Gim J, Kim S and Kim J 2014 Effect of Mo^{6+} doping on electrochemical performance of anatase TiO_2 as a high performance anode material for secondary lithium-ion batteries *J. Alloys Compd.* **598** 16–22
[66] Zhang J, Xi J and Ji Z 2012 Mo^+ N codoped TiO_2 sheets with dominant {001} facets for enhancing visible-light photocatalytic activity *J. Mater. Chem.* **22** 17700–8
[67] López R and Gómez R 2011 Photocatalytic degradation of 4-nitrophenol on well characterized sol–gel molybdenum doped titania semiconductors *Top. Catal.* **54** 504–11
[68] Avilés-García O, Espino-Valencia J, Romero R, Rico-Cerda J L, Arroyo-Albiter M and Natividad R 2017 W and Mo doped TiO_2: synthesis, characterization and photocatalytic activity *Fuel* **198** 31–41
[69] Dorraj M, Goh B T, Sairi N A, Woi P M and Basirun W J 2018 Improved visible-light photocatalytic activity of TiO_2 co-doped with copper and iodine *Appl. Surf. Sci.* **439** 999–1009
[70] Tian F, Zhang Y, Zhang J and Pan C 2012 Raman spectroscopy: a new approach to measure the percentage of anatase TiO_2 exposed (001) facets *J. Phys. Chem.* C **116** 7515–9
[71] Avilés-García O *et al* 2018 Enhanced photocatalytic activity of titania by co-doping with Mo and W *Catalysts* **8** 631
[72] Zhang H, Tan K, Zheng H, Gu Y and Zhang W 2011 Preparation, characterization and photocatalytic activity of TiO_2 codoped with yttrium and nitrogen *Mater. Chem. Phys.* **125** 156–60
[73] Choudhury B and Choudhury A 2012 Dopant induced changes in structural and optical properties of Cr^{3+} doped TiO_2 nanoparticles *Mater. Chem. Phys.* **132** 1112–8
[74] Santara B, Pal B and Giri P 2011 Signature of strong ferromagnetism and optical properties of Co doped TiO_2 nanoparticles *J. Appl. Phys.* **110** 114322
[75] Parker J and Siegel R 1990 Calibration of the Raman spectrum to the oxygen stoichiometry of nanophase TiO_2 *Appl. Phys. Lett.* **57** 943–5
[76] Sun L, Li J, Wang C, Li S, Chen H and Lin C 2009 An electrochemical strategy of doping Fe^{3+} into TiO_2 nanotube array films for enhancement in photocatalytic activity *Sol. Energy Mater. Sol. Cells* **93** 1875–80
[77] Liu S-H and Syu H-R 2012 One-step fabrication of N-doped mesoporous TiO_2 nanoparticles by self-assembly for photocatalytic water splitting under visible light *Appl. Energy* **100** 148–54
[78] Tripathi A K *et al* 2015 Photoluminescence and photoconductivity of Ni doped titania nanoparticles *Adv. Mater. Lett.* **6** 201–8
[79] Choudhury B and Choudhury A 2013 Oxygen vacancy and dopant concentration dependent magnetic properties of Mn doped TiO_2 nanoparticle *Curr. Appl Phys.* **13** 1025–31
[80] Ahmed S 2017 Ferromagnetism in Cr-, Fe-, and Ni-doped TiO_2 samples *J. Magn. Magn. Mater.* **442** 152–7
[81] Yan Y *et al* 2018 Efficient photocatalytic disinfection of *Escherichia coli* by N-doped TiO_2 coated on coal fly ash cenospheres *J. Photochem. Photobiol.* A **367** 355–64
[82] Mecha A, Onyango M, Ochieng A and Momba M 2019 UV and solar photocatalytic disinfection of municipal wastewater: inactivation, reactivation and regrowth of bacterial pathogens *Int. J. Environ. Sci. Technol.* **16** 3687–96
[83] Venieri D *et al* 2014 Solar light and metal-doped TiO_2 to eliminate water-transmitted bacterial pathogens: photocatalyst characterization and disinfection performance *Appl. Catal.* B **154** 93–101
[84] You J, Guo Y, Guo R and Liu X 2019 A review of visible light-active photocatalysts for water disinfection: features and prospects *Chem. Eng. J.* **373** 624–41

[85] Vijay M et al 2013 Photocatalytic inactivation of gram-positive and gram-negative bacteria by reactive plasma processed nanocrystalline TiO_2 powder *Curr. Appl Phys.* **13** 510–6
[86] Ganguly P, Byrne C, Breen A and Pillai S C 2018 Antimicrobial activity of photocatalysts: fundamentals, mechanisms, kinetics and recent advances *Appl. Catal.* B **225** 51–75
[87] Reddy P V L, Kavitha B, Reddy P A K and Kim K-H 2017 TiO_2-based photocatalytic disinfection of microbes in aqueous media: a review *Environ. Res.* **154** 296–303